Robust estimation of Hi-C contact matrices using fused lasso reveals preferential insulation of super-enhancers by strong TAD boundaries

Yixiao Gong[1,2,+], Charalampos Lazaris[1,2,+], Aurelie Lozano[3], Prabhanjan Kambadur[4], Panagiotis Ntziachristos[5], Iannis Aifantis[1,2,*], Aristotelis Tsirigos[1,2,6,*]

[1] Department of Pathology, NYU School of Medicine, New York, NY 10016, USA

[2] Laura and Isaac Perlmutter Cancer Center and Helen L. and Martin S. Kimmel Center for Stem Cell Biology, NYU School of Medicine, New York, NY 10016, USA

[3] Center for Computational and Statistical Learning, IBM T.J. Watson Research Center, NY 10598, USA

[4] Bloomberg LP, 731 Lexington Avenue, New York City, NY, USA

[5] Department of Biochemistry and Molecular Genetics, Feinberg School of Medicine, Northwestern University, Chicago, IL 60611, USA

[6] Applied Bioinformatics Laboratories, NYU School of Medicine, NY 10016, USA

[+] Equal contribution

* To whom correspondence should be addressed. Tel: +16465012693; Email: Aristotelis.Tsirigos@nyumc.org; Correspondence may also be addressed to Iannis Aifantis. Tel: +1 212 263 9898, Fax: +1 212 263 9210, E-mail: Ioannis.Aifantis@nyumc.org

ABSTRACT

The metazoan genome is compartmentalized in megabase-scale areas of highly interacting chromatin known as topologically associating domains (TADs), typically identified by computational analyses of Hi-C sequencing data. TADs are demarcated by boundaries that have been shown to be largely conserved across cell types and even across species. Increasing evidence suggests that the seemingly invariant TADs may exhibit some plasticity in certain cases and their boundary strength can vary. However, a genome-wide

characterization of TAD boundary strength in mammals is still lacking. In this study, we use fused two-dimensional lasso as a machine-learning method to first improve Hi-C contact matrix reproducibility and subsequently categorize TAD boundaries based on their strength. We demonstrate that increased boundary strength is associated with elevated levels of CTCF and that TAD boundary insulation scores may differ across cell types. Intriguingly, we also found that super-enhancer elements are preferentially insulated by strong boundaries. Presumably, genetic or epigenetic inactivation of strong boundaries may lead to loss of insulation around super-enhancers, disrupt the physiological transcriptional program and cause disease.

INTRODUCTION

The advent of proximity-based ligation assays has allowed us to probe three-dimensional chromatin organization at unprecedented resolution [1, 2]. Hi-C, a high-throughput chromosome conformation variant has allowed genome-wide identification of chromatin-chromatin interactions [3]. Hi-C is prone to biases and multiple algorithms have been developed for Hi-C bias correction, including probabilistic modelling methods [4], Poisson or negative binomial normalization [5] and the widely popular Iterative Correction and Eigenvalue decomposition method (ICE) [6], which assumes “equal visibility” of genomic loci. A similar iterative method named Sequential Component Normalization was introduced by Cournac *et al.* [7]. Additional efficient correction methods have been developed to handle high-resolution Hi-C datasets [8]. Hi-C has revealed that the metazoan genome is organized in areas of active and inactive chromatin known as A and B compartment respectively [3]. These are further compartmentalized in super-TADs [9], topologically associating domains (TADs) [10–12] and sub-TADs [13], as well as gene neighbourhoods [14]. Some algorithms have been already developed to reveal this hierarchical chromatin organization, including Directionality Index (DI) [10], Armatus [15], TADtree [16], Insulation Index (Crane) [17], IC-Finder [18] and others. TADs are megabase-scale areas of highly interacting chromatin, demarcated by CTCF-enriched boundaries, and are highly-conserved across species and cell types [10, 19].

55 Genome compartmentalization in TADs confines enhancer-promoter interactions within the
56 same domain [10, 12, 20] and during cell differentiation most changes have been shown to
57 occur within TADs [21]. TAD boundaries have been found to be rich in tRNA genes,
58 transposable elements, CCCTC-binding factor (CTCF), cohesin complex and other structural
59 proteins [10–12]. More recently, proteins involved in chromatin remodelling such as BRG1 –
60 an ATPase driving SWI/SNF activity – as well topoisomerase complexes have been implicated
61 in boundary formation through regulation of chromatin compaction [22]. Whereas TADs are
62 seemingly invariant, mounting evidence suggests that TAD boundaries can vary in strength,
63 ranging from permissive TAD boundaries that allow more inter-TAD interactions to more rigid
64 (strong) boundaries that clearly demarcate adjacent TADs [23]. Recent studies have shown
65 that in *Drosophila*, exposure to heat-shock resulted in local changes in certain TAD boundaries
66 resulting in TAD merging which is believed to have physiological consequences [24]. A recent
67 study in mammals showed that during motor neuron (MN) differentiation in mammals, TAD
68 and sub-TAD boundaries in *Hox* cluster are not rigid and their plasticity is linked to changes
69 in the expression of genes of the *Hox* cluster during differentiation [25]. It has also been
70 demonstrated that boundary strength is positively associated with the occupancy of certain
71 structural proteins including CCCTC-binding factor (CTCF) [10]. Despite the fact that there is
72 a handful of studies demonstrating that not all boundaries are equal and they can vary in
73 strength in organisms like *Drosophila*, no study has yet addressed the issue of boundary
74 strength in mammals and how it may be related to potential boundary disruptions and aberrant
75 gene activation in diseases like cancer. Here we introduce a new method based on fused two-
76 dimensional lasso [26] in order to: (a) to improve the correlation of Hi-C contact matrices, (b)
77 reveal the multiple levels of chromatin organization and (c) categorize TAD boundaries based
78 on their corresponding strength.
79

80 **MATERIALS AND METHODS**

81 **Hi-C datasets**

In order to develop a method that successfully handles variation in Hi-C data and improves reproducibility, we carefully selected our Hi-C datasets to represent technical variation due to the execution of the experiments by different laboratories and/or the usage of different enzymes. We ensured that our datasets included samples at least ~40 million intra-chromosomal read pairs and that the Hi-C experiment was performed in biological replicates, either by using one restriction enzyme (HindIII or MboI) (H1 cells and their derivatives [21], K562, KBM7 and NHEK cells [27] and in-house generated CUTLL-1), or two enzymes (HindIII or MboI) (GM12878 [27], IMR90 [10, 28]), in order to examine the consistency of predicted Hi-C interactions across different enzymes.

Calculation of same-enzyme and cross-enzyme correlations

We calculated two types of correlation for Hi-C matrices, to evaluate the performance of our method. The two types of correlation were: a) same-enzyme correlation which corresponds to all the Hi-C replicates prepared with the same restriction enzyme, b) cross-enzyme correlation which corresponds to all the sample pairs where the same Hi-C sample was prepared with two different enzymes (e.g HindIII/MboI). Pearson correlation coefficients were calculated either on the filtered, ICE-corrected [6] or scaled (see below) Hi-C contact matrices (Pearson) or the distance normalized ones (Pearson (*z*-score)).

Generation of scaled Hi-C contact matrices

In order to improve the cross-enzyme (and same-enzyme) correlation of Hi-C matrices we accounted for the total number of read pairs and the "effective length" [4]. More specifically, the scaled number of reads corresponding to interactions between the Hi-C matrix bins *i,j* (y_{ij}) is defined by the formula:

$$y_{ij} = \frac{x_{ij}}{eff_i \cdot eff_j \cdot N}$$

where x_{ij} is the original number of interactions between the bins *i* and *j*, eff_i the effective length for the bin *i*, eff_j the effective length for the bin j, and *N* is the total number of read pairs.

108 **Distance normalization**

109 Genomic loci that are further apart in terms of linear distance on DNA tend to give fewer
110 interactions in Hi-C maps than loci that are closer. For intra-chromosomal interactions, this
111 effect of genomic distance should be taken into account. Consequently, the interactions were
112 distance-normalized using a *z*-score that was calculated taking into account the mean Hi-C
113 counts for all interactions at a given distance *d* and the corresponding standard deviation.
114 Thus, the *z*-score for the interaction between the Hi-C contact matrix bins *i* and *j* (z_{ij}) is given
115 the following equation:

116 $$z_{ij} = \frac{y_{ij} - \mu(d)}{\sigma(d)}$$

117 where y_{ij} corresponds to the number of interactions between the bins *i* and *j*, $\mu(d)$ to the mean
118 (expected) number of interactions for distance d=|j-i| and $\sigma(d)$ is the corresponding standard
119 deviation of the mean. The higher the difference between the observed (y_{ij}) and expected
120 number of interactions ($\mu(d)$), the higher the corresponding *z*-score.

121 **Fused two-dimensional lasso**

122 While our naïve scaling approach successfully increased the cross-enzyme and same-
123 enzyme correlation of Hi-C matrices, we sought to improve the correlation even further. We
124 used two-dimensional lasso, an optimization machine learning technique widely used to
125 analyse noisy datasets, especially images [26]. This technique is very-well suited for
126 identifying topological domains based on contact maps generated by Hi-C sequencing
127 experiments for two reasons: (a) Hi-C datasets are inherently noisy, and (b) topological
128 domains are continuous DNA segments of highly interacting loci that would represent solid
129 squares along the diagonal of Hi-C contact matrices. Topological domains map to squares of
130 different length along the diagonal of the Hi-C contact matrix, but they are not solid as they
131 contain several gaps, i.e. scattered regions on those squares that show little or no interaction.
132 Two-dimensional fused lasso addresses the issue by penalizing differences between
133 neighbouring elements in the contact matrix. This is achieved by the penalty parameter λ
134 (lambda), as described in the equation:

$$\hat{\beta} = \underset{\beta \in \mathbb{R}^n}{\operatorname{argmin}} \frac{1}{2} \sum_{i=1}^{n} (y_i - \beta_i)^2 + \lambda \sum_{(i,j) \in E} \left| \beta_i - \beta_j \right| ,$$

where y is the original (i.e. observed) contact matrix, and $\hat{\beta}$ is the estimated contact matrix such that the objective function described above in minimized. In the interest of computational efficiency, we applied one-dimensional lasso on the Hi-C contact matrices in order to estimate the matrices for high values of λ and obtain the full hierarchy of TAD boundaries. Using one-dimensional lasso instead of the two-dimensional version had no negative impact on the correlations of Hi-C contact matrices between replicates (**Supplemental Figure 1**).

Classification of boundaries based on fused two-dimensional lasso

We applied two-dimensional fused lasso to categorize TAD boundaries based on their strength. The rationale behind this categorization is that topological domains separated by more "permissive" (i.e. weaker) boundaries [29] will tend to fuse into larger domains when lasso is applied, compared to TADs separated by well-defined, stronger boundaries. We indeed applied this strategy and categorized boundaries into multiple groups ranging from the most permissive to the strongest boundaries. The boundaries that were lost when λ value was increased from 0 to 0.25, fall in the first category (λ=0), the ones lost when λ was increased to 0.5, in the second (λ=0.2) etc.

Association of CTCF levels with boundary strength

We obtained CTCF ChIP-sequencing data for the cell lines utilized in this study (with the exception of KBM7 for which no publicly available dataset was available) and we uniformly re-processed all data using HiC-bench [30]**.** Total CTCF levels at each TAD boundary were calculated and their normalized distributions for each boundary category (weak to strong) were plotted in boxplots in order to demonstrate the association of increased boundary strength with increased levels of CTCF binding.

Association of boundary strength with super-enhancers and repeat elements

162 Super-enhancers were called using H3K27ac ChIP-seq data from GEO, ENCODE and in-
163 house generated data. Reads were first aligned with Bowtie2 v2.3.1 [31] and then HOMER
164 v4.6 [32] was used to call super-enhancers, all with standard parameters. For each super-
165 enhancer in each sample, we identified the corresponding TAD and its TAD boundaries. We
166 then counted (per sample) the percentage of super-enhancers that are surrounded by
167 boundaries belonging in each boundary category, demonstrating that most super-enhancers
168 are insulated by strong boundaries.
169

170 **RESULTS**

171 **Comprehensive re-analysis of published high-resolution Hi-C datasets**

172 We identified publicly available human Hi-C datasets (described in Materials and Methods
173 section) that fulfilled the following criteria: (i) two biological replicates and (ii) sufficient
174 sequencing depth to robustly identify topologically-associating domains (TADs) as described
175 in our TAD calling benchmark study [30]. All datasets were then comprehensively re-analysed
176 using HiC-bench. Quality assessment analysis revealed that the samples varied considerably
177 in terms of total numbers of reads, ranging from ~150 million reads to more than 1.3 billion
178 (**Figure 1A**). Mappable reads were over 96% in all samples. The percentages of total accepted
179 reads corresponding to *cis* (ds-accepted-intra, dark green) and *trans* (ds-accepted-inter, light
180 green) (**Figure 1B**) also varied widely, ranging from ~17% to ~56%. Duplicate read pairs (*ds-*
181 *duplicate-intra* and *ds-duplicate-inter*; red and pink respectively), non-uniquely mappable
182 (*multihit*; light blue), single-end mappable (*single-sided*; dark blue) and unmapped reads
183 (*unmapped*; dark purple) were discarded. Self-ligation products (*ds-same-fragment*; orange)
184 and reads mapping too far (*ds-too-far*; light purple) from restriction sites or too close to one
185 another (*ds-too-close*; orange) were also discarded. Only double-sided uniquely mappable *cis*
186 (*ds-accepted-intra*; dark green) and *trans* (*ds-accepted-inter*; light green) read pairs were used
187 for downstream analysis. Despite the differences in sequencing depth and in the percentages
188 of useful reads across samples, all samples had enough useful reads for TAD calling and thus
189 none of them was excluded from downstream analysis. However, due to the wide differences

190 in sequencing depth, and to ensure fair comparisons of Hi-C matrices in this study, all datasets
191 were down-sampled such that the number of usable intra-chromosomal reads pairs was ~40
192 million for each replicate.
193
194 **Assessment of same-enzyme and cross-enzyme reproducibility of Hi-C contact**
195 **matrices**
196 Although it has been demonstrated in the literature that Hi-C libraries are prone to enzyme
197 biases (see Introduction), no systematic large-scale study has investigated in detail the
198 reproducibility of Hi-C contact matrices. Here, we attempt to address this question using the
199 most comprehensive Hi-C dataset that is currently available, as described in the previous
200 section. More specifically, we will focus on multiple factors that may play an important role on
201 reproducibility: first, we will separately consider biological replicates of Hi-C libraries generated
202 with the same or different restriction enzymes; second, we will study the impact of Hi-C matrix
203 resolution (i.e. bin size); third, we will assess reproducibility as a function of the distance of
204 interacting loci pairs. Pearson correlation coefficients were calculated for each pair of
205 replicates (same- or cross-enzyme) on Hi-C contact matrices estimated by three methods: (i)
206 naïve filtering (i.e. matrix generation by simply using double-sided accepted intra-
207 chromosomal read pairs from **Figure 1A**), (ii) iterative correction (ICE) which has already been
208 demonstrated to improve cross-enzyme correlation, and (iii) our own simple scaling method
209 that only corrects for effective length bias (see Methods for details). Importantly, correlations
210 were computed both on the actual matrices, but also on the distance-normalized matrices (see
211 Methods for details), as Hi-C interactions are typically concentrated around the diagonal of the
212 Hi-C contact matrix, and values are dropping exponentially as the distance between the
213 interacting pairs is increasing. Distance-normalized matrices account for the expected Hi-C
214 read count as a function of distance and may therefore reveal real distal interactions. The
215 results of our benchmark analysis are summarized in **Figure 1C**: the left panel summarizes
216 the correlations between replicates generated by the same restriction enzyme, whereas the
217 right panel the correlations between replicates generated by a different restriction enzymes.

In both scenarios, as expected, correlations drop quickly as finer resolutions (from 100kb to 20kb) are considered, especially in the distance-normalized matrices. The same conclusion applies for increasing distance (from 2Mb to 10Mb) between interacting loci, demonstrating that long-range interactions require ultra-deep sequencing in order to be detected reliably. To elaborate on this point, we repeated the analysis after retaining only those samples with two replicates of at least 70 million or 110 million usable intra-chromosomal reads and resampling them down to 80 million or 120 million per replicate (**Supplemental Figure 2** and **Supplemental Figure 3** respectively). Both conclusions hold true with the new sequencing depth and are independent of the Hi-C contact matrix estimation method. Finally, bias-correction methods (ICE and our scaling approach) indeed improved cross-enzyme correlation over the naïve filtering method. Interestingly, this improvement came at the expense of lower correlations in the same-enzyme case. More specifically, we observed that the largest the gain in cross-enzyme correlations, the greater the loss in same-enzyme correlations (ICE method) (**Figure 1C**).

Fused lasso improves same-enzyme and cross-enzyme correlations of Hi-C contact matrices

Motivated by the poor performance of all methods at fine resolutions and by the observation of a surprising trade-off between improving cross-enzyme at the expense of lower same-enzyme correlation when correcting for enzyme-related biases, we applied fused two-dimensional lasso (see Methods for details), a well-studied image denoising method, to generate Hi-C contact matrices with increased consistency between replicates. Briefly, two-dimensional fused lasso utilized a parameter λ which penalizes differences between neighboring values in the Hi-C contact matrix. The effect of parameter λ is demonstrated in **Figure 2A** where we show an example of the application of fused two-dimensional lasso on a Hi-C contact matrix focused on an 8Mb locus on chromosome 8 for different values of parameter λ. To evaluate the performance of fused lasso, as done in the previous section, we calculated same-enzyme and cross-enzyme Pearson correlations between Hi-C contact

246 matrices generated from different replicates. Pearson correlation coefficients were calculated
247 either for iteratively-corrected (ICE) or scaled Hi-C contact matrices and compared to the naïve
248 filtering approach. The results are summarized in **Figure 2B**. Clearly, increasing λ improves
249 correlation independent of resolution, restriction enzyme and bias-correction method,
250 demonstrating the robustness of our approach. Similarly, fused two-dimensional lasso
251 improves the reproducibility of distance-normalized matrices as demonstrated in **Figure 3**.
252

253 **Fused lasso reveals a TAD hierarchy linked to TAD boundary strength**

254 After demonstrating that parameter λ helps improve reproducibility of Hi-C contact matrices
255 independent of the bias-correction method, we further hypothesized that increased values of
256 λ may define distinct classes of TADs with different properties. For this reason, we now allowed
257 λ to range from 0 to the maximum possible value (after a finite value of λ, the entire Hi-C matrix
258 attains a constant value independent of the value of λ). For efficient computation, we used a
259 one-dimensional approximation of the two-dimensional lasso solution (see Methods for details
260 and **Supplemental Figure 1**). We then identified TADs at multiple λ values using HiC-bench,
261 and we observed that the number of TADs is monotonically decreasing with the value of λ
262 (**Figure 4A**), suggesting that by increasing λ, we are effectively identifying larger TADs
263 encompassing smaller TADs detected at smaller λ values. Equivalently, certain TAD
264 boundaries "disappear" as λ is increased. Therefore, we hypothesized that TAD boundaries
265 that disappear at lower values of λ are weaker (i.e. lower insulation score) whereas boundaries
266 that disappear at higher values of λ are stronger (i.e. higher insulation score). To test this
267 hypothesis, we identified the TAD boundaries that are "lost" at each value of λ, and generated
268 the distributions of the insulation scores as defined by the ratio score described in HiC-bench.
269 Indeed, as hypothesized, TAD boundaries lost at higher values of parameter λ are associated
270 with higher TAD insulation scores (**Figure 4B**). We then stratified TAD boundaries into six
271 classes according to their strength, independently in each Hi-C dataset used in this study and
272 generated a heatmap representation including all TAD boundaries and their associated class
273 across all samples (**Figure 4C,D**). Hierarchical clustering correctly grouped replicates and

related cell types independent of enzyme biases or batch effects related to the lab that generated the Hi-C libraries, suggesting that TAD boundary strength can be used to distinguish cell types. Equivalently, this finding suggests, although TAD boundaries have been shown to be largely invariant across cell types, a certain subset of TAD boundaries may exhibit varying degrees of strength in different cell types. As expected, TAD boundary strength was found to be positively associated with CTCF levels, suggesting that stronger CTCF binding confers stronger insulation (**Figure 4E**). SINE elements have also been shown to be enriched at TAD boundaries [10], and apart from confirming this finding, we extended it and demonstrated that Alu elements (the most abundant type of SINE elements) are enriched at stronger TAD boundaries, whereas, interestingly, L1 elements (a subset of LINE elements) are enriched at weaker TAD boundaries (**Figure 4F**). A comprehensive analysis of all major repetitive element subtypes can be found in **Supplemental Figure 4**. Finally, we investigated the proximity of super-enhancers to TAD boundaries of different strength. Intriguingly, we found that super-enhancers are preferentially insulated by strong TAD boundaries (**Figure 4G**). Super-enhancers are thought to be cell specific and drive expression of key genes. Thus, a potential explanation of our finding is that super-enhancers should only target genes confined in the same TAD, while strongly insulated from genes in adjacent TADs. Genetic or epigenetic inactivation of strong boundaries may lead to loss of insulation around super-enhancers, disrupt the physiological transcriptional program and cause disease.

DISCUSSION

Multiple recent studies have revealed that the metazoan genome is compartmentalized in boundary-demarcated functional units known as topologically associating domains (TADs). TADs are highly conserved across species and cell types. A few studies, however, provide compelling evidence that specific TADs, despite the fact that they are largely invariant, exhibit some plasticity. Given that TAD boundary disruption has been recently linked to aberrant gene activation and multiple disorders including developmental defects and cancer, categorization of boundaries based on their strength and identification of their unique features becomes of

302 particular importance. In this study, we developed a method based on fused two-dimensional
303 lasso in order to categorize TAD boundaries based on their strength. We demonstrated that
304 our method: (a) improves the correlation of Hi-C contact matrices irrespective of the Hi-C bias
305 correction method used, (b) reveals multiple levels of chromatin organization and (c)
306 successfully identifies boundaries of variable strength and that strong predicted boundaries
307 exhibit certain expected features, such as elevated CTCF levels and increased insulating
308 capacity. We also demonstrated that the boundaries of similar strength are largely conserved
309 across the samples included in this study, however, a subset of TAD boundaries displays
310 varying levels of insulation strength across samples. By performing an integrative analysis of
311 estimated boundary strength with super-enhancers in matched samples, we observed that
312 super-enhancers are preferentially insulated by strong boundaries. Based on this observation,
313 we believe that strong boundaries prevent the aberrant activation of genes residing in adjacent
314 TADs, by consisting a physical barrier between the gene promoters and the super-enhancer
315 elements. We predict that despite the fact that weak boundaries would be more prone to
316 disruption, in many cancers, strong boundaries are actually disrupted by either genetic lesions
317 or epigenetically, leading to aberrant activation of oncogenes by enhancers as recently
318 demonstrated [33–36]. In future work, we will further characterize boundaries of variable
319 strength, reveal their features and help with the identification of targets for pharmacological
320 intervention, in order to restore disrupted boundaries.
321

322 **AUTHOR CONTRIBUTIONS**

323 YG and CL performed computational analyses and generated figures. AT, AL and PK
324 conceived this study. PN performed the CUTLL-1 Hi-C experiments. PN and IA offered
325 biological insights and helped with the interpretation of Hi-C data. AT designed and
326 implemented the method. CL and AT wrote the manuscript. All authors read and approved the
327 final manuscript.

328

ACKNOWLEDGEMENTS

We would like to thank all members of the Tsirigos and Aifantis Laboratories for critical evaluation of the manuscript. We would like to thank the Applied Bioinformatics Laboratories (ABL) at the NYU School of Medicine for providing bioinformatics support and helping with the analysis and interpretation of the data. This work has used computing resources at the NYU High Performance Computing Facility (HPCF). We also thank the Genome Technology Center (GTC) for expert library preparation and sequencing. This shared resource is partially supported by the Cancer Center Support Grant, P30CA016087, at the Laura and Isaac Perlmutter Cancer Center.

FUNDING

The study was supported by the American Cancer Society [RSG-15-189-01-RMC to AT] and a Leukemia & Lymphoma Society New Idea Award [8007-17 to AT]. NYU Genome Technology Center (GTC) is a shared resource, partially supported by the Cancer Center Support Grant [P30CA016087] at the Laura and Isaac Perlmutter Cancer Center.

TABLE AND FIGURES LEGENDS

Figure 1: Assessment of the reproducibility of Hi-C contact matrices across biological replicates. **(A)** Counts of Hi-C read pairs in various read categories: dark and light green indicate read pairs that were not designated as artifacts and can be used in downstream analyses, **(B)** Percentages of Hi-C reads in each category, **(C)** Comparison of Hi-C contact matrices between biological replicates generated from Hi-C library using the same or different restriction enzyme; Hi-C matrices were estimated using three methods (naïve filtering, iterative correction and simple scaling); assessment was performed using Pearson correlation on the actual or distance-normalized Hi-C matrices at resolutions ranging from 100kb to 20kb and maximum distances of 2Mb, 6Mb and 10Mb between interacting pairs

Figure 2: Fused two-dimensional lasso improves reproducibility of Hi-C contact matrices. **(A)** Example of application of fused two-dimensional lasso on a Hi-C contact matrix focused on a 8Mb locus on chromosome 8 for different values of parameter λ, **(B)** Hi-C contact matrix correlations are improved by increasing the value of fused lasso parameter λ both for matrices estimated by ICE as well as by our simple scaling method; correlations of Hi-C contact matrices generated by the naïve filtering method are marked by the red line in each panel.

Figure 3: Fused two-dimensional lasso improves reproducibility of distance-normalized Hi-C contact matrices. **(A)** Example of application of fused two-dimensional lasso on a distance-normalized Hi-C contact matrix focused on an 8Mb locus on chromosome 8 for different values of parameter λ, **(B)** distance-normalized Hi-C contact matrix correlations are improved by increasing the value of fused lasso parameter λ both for matrices estimated by ICE as well as by our simple scaling method; correlations of distance-normalized Hi-C contact matrices generated by the naïve filtering method are marked by the red line in each panel. The gradient of blue corresponds to λ values with darker blue denoting higher λ value.

Figure 4: Classification and characterization of TAD boundaries according to insulation score. **(A)** Number of TADs for λ values ranging from 0 to 5, **(B)** TAD boundaries lost at higher values of parameter λ are associated with higher TAD insulation scores, **(C)** heatmap representation of TAD boundary insulation strength across samples; hierarchical clustering correctly groups replicates and related cell types independent of enzyme biases or batch effects related to the lab that generated the Hi-C libraries, **(D)** Classification of boundaries according to boundary strength across samples, **(E)** TAD boundary strength is associated with CTCF levels, **(F)** Alu elements are enriched at stronger TAD boundaries whereas L1 elements are enriched at weaker TAD boundaries, **(G)** Super-enhancers are preferentially insulated by stronger TAD boundaries. The gradient of blue corresponds to λ values with darker blue denoting higher λ value.

380 **Supplementary Figure 1:** Comparison of Hi-C contact matrices between biological replicates
381 generated from Hi-C library using the same restriction enzyme. Three methods (naïve filtering,
382 iterative correction and simple scaling) were used for estimation. Assessment was performed
383 using Pearson correlation on the actual or distance-normalized Hi-C matrices at resolutions
384 ranging from 100kb to 20kb and maximum distances of 2Mb, 6Mb and 10Mb between
385 interacting pairs. Only samples with approximately 80 million usable intra-chromosomal reads
386 were considered.

387 **Supplementary Figure 2:** Comparison of Hi-C contact matrices between biological replicates
388 generated from Hi-C library using the same restriction enzyme. Three methods (naïve filtering,
389 iterative correction and simple scaling) were used for estimation. Assessment was performed
390 using Pearson correlation on the actual or distance-normalized Hi-C matrices at resolutions
391 ranging from 100kb to 20kb and maximum distances of 2Mb, 6Mb and 10Mb between
392 interacting pairs. Only samples with approximately 120 million usable intra-chromosomal
393 reads were considered.

394 **Supplementary Figure 3:** Fused one-dimensional lasso improves reproducibility of distance-
395 normalized Hi-C contact matrices. **(A)** Hi-C contact matrix and **(B)** distance-normalized Hi-C
396 contact matrix correlations are improved by increasing the value of fused lasso parameter λ
397 both for matrices estimated by ICE as well as by our simple scaling method; correlations of
398 distance-normalized Hi-C contact matrices generated by the naïve filtering method are marked
399 by the red line in each panel. The gradient of blue corresponds to λ values with darker blue
400 denoting higher λ value.

401 **Supplementary Figure 4:** Numbers of repeat elements in proximity to boundaries of certain
402 boundary strength. Darker blue in the blue colour gradient denotes higher boundary strength.

403

404

405 **REFERENCES**

406 1. Dekker J, Marti-Renom MA, Mirny LA. Exploring the three-dimensional organization of
407 genomes: interpreting chromatin interaction data. Nat Rev Genet. 2013;14:390–403.
408 doi:10.1038/nrg3454.

409 2. Schmitt AD, Hu M, Ren B. Genome-wide mapping and analysis of chromosome
410 architecture. Nat Rev Mol Cell Biol. 2016;17:743–55. doi:10.1038/nrm.2016.104.

411 3. Lieberman-Aiden E, van Berkum NL, Williams L, Imakaev M, Ragoczy T, Telling A, et al.
412 Comprehensive mapping of long-range interactions reveals folding principles of the human
413 genome. Science. 2009;326:289–93. doi:10.1126/science.1181369.

414 4. Yaffe E, Tanay A. Probabilistic modeling of Hi-C contact maps eliminates systematic
415 biases to characterize global chromosomal architecture. Nat Genet. 2011;43:1059–65.
416 doi:10.1038/ng.947.

417 5. Hu M, Deng K, Selvaraj S, Qin Z, Ren B, Liu JS. HiCNorm: removing biases in Hi-C data
418 via Poisson regression. Bioinformatics. 2012;28:3131–3. doi:10.1093/bioinformatics/bts570.

419 6. Imakaev M, Fudenberg G, McCord RP, Naumova N, Goloborodko A, Lajoie BR, et al.
420 Iterative correction of Hi-C data reveals hallmarks of chromosome organization. Nat
421 Methods. 2012;9:999–1003. doi:10.1038/nmeth.2148.

422 7. Cournac A, Marie-Nelly H, Marbouty M, Koszul R, Mozziconacci J. Normalization of a
423 chromosomal contact map. BMC Genomics. 2012;13:436. doi:10.1186/1471-2164-13-436.

424 8. Knight PA, Ruiz D. A fast algorithm for matrix balancing. IMA Journal of Numerical
425 Analysis. 2013;33:1029–47. doi:10.1093/imanum/drs019.

426 9. Fraser J, Ferrai C, Chiariello AM, Schueler M, Rito T, Laudanno G, et al. Hierarchical
427 folding and reorganization of chromosomes are linked to transcriptional changes in cellular
428 differentiation. Mol Syst Biol. 2015;11:852. doi:10.15252/msb.20156492.

429 10. Dixon JR, Selvaraj S, Yue F, Kim A, Li Y, Shen Y, et al. Topological domains in
430 mammalian genomes identified by analysis of chromatin interactions. Nature. 2012;485:376–
431 80. doi:10.1038/nature11082.

432 11. Nora EP, Lajoie BR, Schulz EG, Giorgetti L, Okamoto I, Servant N, et al. Spatial
433 partitioning of the regulatory landscape of the X-inactivation centre. Nature. 2012;485:381–5.
434 doi:10.1038/nature11049.

435 12. Sexton T, Yaffe E, Kenigsberg E, Bantignies F, Leblanc B, Hoichman M, et al. Three-
436 dimensional folding and functional organization principles of the Drosophila genome. Cell.
437 2012;148:458–72. doi:10.1016/j.cell.2012.01.010.

438 13. Phillips-Cremins JE, Sauria ME, Sanyal A, Gerasimova TI, Lajoie BR, Bell JS, et al.
439 Architectural protein subclasses shape 3D organization of genomes during lineage
440 commitment. Cell. 2013;153:1281–95. doi:10.1016/j.cell.2013.04.053.

441 14. Dowen JM, Fan ZP, Hnisz D, Ren G, Abraham BJ, Zhang LN, et al. Control of cell

442 identity genes occurs in insulated neighborhoods in mammalian chromosomes. Cell.
443 2014;159:374–87. doi:10.1016/j.cell.2014.09.030.

444 15. Filippova D, Patro R, Duggal G, Kingsford C. Identification of alternative topological
445 domains in chromatin. Algorithms Mol Biol. 2014;9:14. doi:10.1186/1748-7188-9-14.

446 16. Weinreb C, Raphael BJ. Identification of hierarchical chromatin domains. Bioinformatics.
447 2016;32:1601–9. doi:10.1093/bioinformatics/btv485.

448 17. Crane E, Bian Q, McCord RP, Lajoie BR, Wheeler BS, Ralston EJ, et al. Condensin-
449 driven remodelling of X chromosome topology during dosage compensation. Nature.
450 2015;523:240–4. doi:10.1038/nature14450.

451 18. Haddad N, Vaillant C, Jost D. IC-Finder: inferring robustly the hierarchical organization of
452 chromatin folding. Nucleic Acids Res. 2017. doi:10.1093/nar/gkx036.

453 19. Vietri Rudan M, Barrington C, Henderson S, Ernst C, Odom DT, Tanay A, et al.
454 Comparative Hi-C reveals that CTCF underlies evolution of chromosomal domain
455 architecture. Cell Rep. 2015;10:1297–309. doi:10.1016/j.celrep.2015.02.004.

456 20. Schoenfelder S, Furlan-Magaril M, Mifsud B, Tavares-Cadete F, Sugar R, Javierre BM,
457 et al. The pluripotent regulatory circuitry connecting promoters to their long-range interacting
458 elements. Genome Res. 2015;25:582–97. doi:10.1101/gr.185272.114.

459 21. Dixon JR, Jung I, Selvaraj S, Shen Y, Antosiewicz-Bourget JE, Lee AY, et al. Chromatin
460 architecture reorganization during stem cell differentiation. Nature. 2015;518:331–6.
461 doi:10.1038/nature14222.

462 22. Barutcu AR, Lian JB, Stein JL, Stein GS, Imbalzano AN. The connection between BRG1,
463 CTCF and topoisomerases at TAD boundaries. Nucleus. 2017;8:150–5.
464 doi:10.1080/19491034.2016.1276145.

465 23. Cubeñas-Potts C, Corces VG. Topologically Associating Domains: An invariant
466 framework or a dynamic scaffold? Nucleus. 2015;6:430–4.
467 doi:10.1080/19491034.2015.1096467.

468 24. Li L, Lyu X, Hou C, Takenaka N, Nguyen HQ, Ong CT, et al. Widespread rearrangement
469 of 3D chromatin organization underlies polycomb-mediated stress-induced silencing. Mol
470 Cell. 2015;58:216–31. doi:10.1016/j.molcel.2015.02.023.

471 25. Narendra V, Bulajić M, Dekker J, Mazzoni EO, Reinberg D. CTCF-mediated topological
472 boundaries during development foster appropriate gene regulation. Genes Dev.
473 2016;30:2657–62. doi:10.1101/gad.288324.116.

474 26. Friedman J, Hastie T, Höfling H, Tibshirani R. Pathwise coordinate optimization. Ann
475 Appl Stat. 2007;1:302–32. doi:10.1214/07-AOAS131.

476 27. Rao SS, Huntley MH, Durand NC, Stamenova EK, Bochkov ID, Robinson JT, et al. A 3D
477 map of the human genome at kilobase resolution reveals principles of chromatin looping.
478 Cell. 2014;159:1665–80. doi:10.1016/j.cell.2014.11.021.

479 28. Jin F, Li Y, Dixon JR, Selvaraj S, Ye Z, Lee AY, et al. A high-resolution map of the three-

480 dimensional chromatin interactome in human cells. Nature. 2013;503:290–4.
481 doi:10.1038/nature12644.

482 29. Rocha PP, Raviram R, Bonneau R, Skok JA. Breaking TADs: insights into hierarchical
483 genome organization. Epigenomics. 2015;7:523–6. doi:10.2217/epi.15.25.

484 30. Lazaris C, Kelly S, Ntziachristos P, Aifantis I, Tsirigos A. HiC-bench: comprehensive and
485 reproducible Hi-C data analysis designed for parameter exploration and benchmarking. BMC
486 Genomics. 2017;18:22. doi:10.1186/s12864-016-3387-6.

487 31. Langmead B, Salzberg SL. Fast gapped-read alignment with Bowtie 2. Nat Methods.
488 2012;9:357–9. doi:10.1038/nmeth.1923.

489 32. Heinz S, Benner C, Spann N, Bertolino E, Lin YC, Laslo P, et al. Simple combinations of
490 lineage-determining transcription factors prime cis-regulatory elements required for
491 macrophage and B cell identities. Mol Cell. 2010;38:576–89.
492 doi:10.1016/j.molcel.2010.05.004.

493 33. Lupiáñez DG, Kraft K, Heinrich V, Krawitz P, Brancati F, Klopocki E, et al. Disruptions of
494 topological chromatin domains cause pathogenic rewiring of gene-enhancer interactions.
495 Cell. 2015;161:1012–25. doi:10.1016/j.cell.2015.04.004.

496 34. Flavahan WA, Drier Y, Liau BB, Gillespie SM, Venteicher AS, Stemmer-Rachamimov
497 AO, et al. Insulator dysfunction and oncogene activation in IDH mutant gliomas. Nature.
498 2016;529:110–4. doi:10.1038/nature16490.

499 35. Hnisz D, Weintraub AS, Day DS, Valton AL, Bak RO, Li CH, et al. Activation of proto-
500 oncogenes by disruption of chromosome neighborhoods. Science. 2016;351:1454–8.
501 doi:10.1126/science.aad9024.

502 36. Weischenfeldt J, Dubash T, Drainas AP, Mardin BR, Chen Y, Stütz AM, et al. Pan-
503 cancer analysis of somatic copy-number alterations implicates IRS4 and IGF2 in enhancer
504 hijacking. Nat Genet. 2017;49:65–74. doi:10.1038/ng.3722.

505

Figure 1

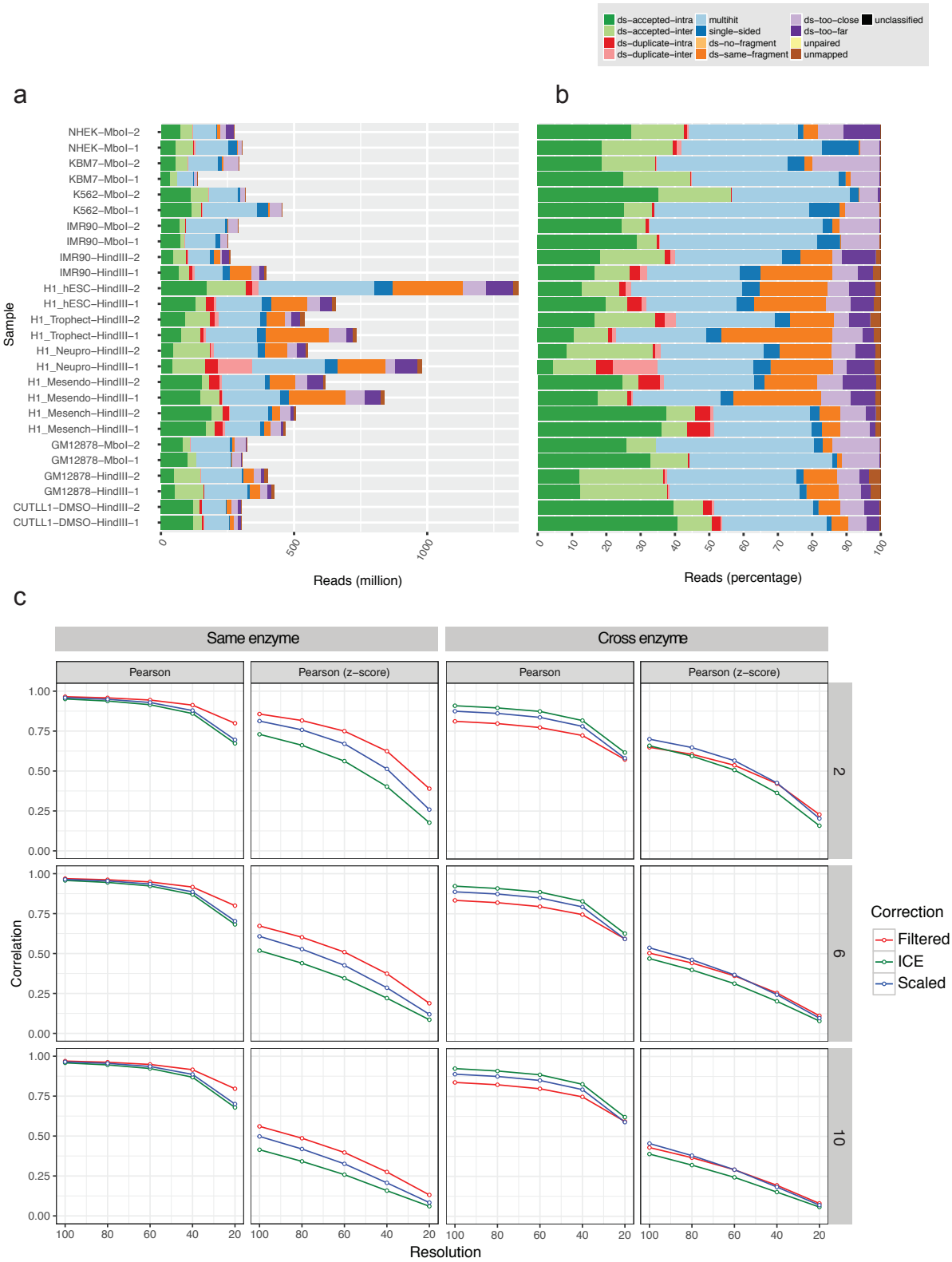
ds−accepted−intra
ds−accepted−inter
ds−duplicate−intra
ds−duplicate−inter
multihit
single−sided
ds−no−fragment
ds−same−fragment
ds−too−close
ds−too−far
unpaired
unmapped
unclassified
a
b
Sample
NHEK−MboI−2
NHEK−MboI−1
KBM7−MboI−2
KBM7−MboI−1
K562−MboI−2
K562−MboI−1
IMR90−MboI−2
IMR90−MboI−1
IMR90−HindIII−2
IMR90−HindIII−1
H1_hESC−HindIII−2
H1_hESC−HindIII−1
H1_Trophect−HindIII−2
H1_Trophect−HindIII−1
H1_Neupro−HindIII−2
H1_Neupro−HindIII−1
H1_Mesendo−HindIII−2
H1_Mesendo−HindIII−1
H1_Mesench−HindIII−2
H1_Mesench−HindIII−1
GM12878−MboI−2
GM12878−MboI−1
GM12878−HindIII−2
GM12878−HindIII−1
CUTLL1−DMSO−HindIII−2
CUTLL1−DMSO−HindIII−1
0
500
1000
Reads (million)
0
10
20
30
40
50
60
70
80
90
100
Reads (percentage)
c
Same enzyme
Cross enzyme
Pearson
Pearson (z−score)
Pearson
Pearson (z−score)
Correlation
1.00
0.75
0.50
0.25
0.00
2
6
10
100
80
60
40
20
Resolution
Correction
Filtered
ICE
Scaled

Figure 2

a

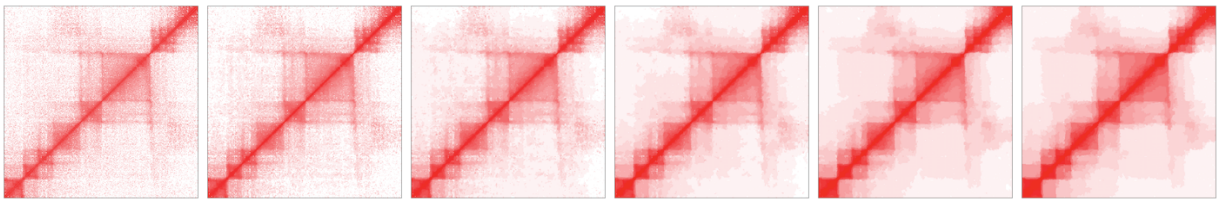

b

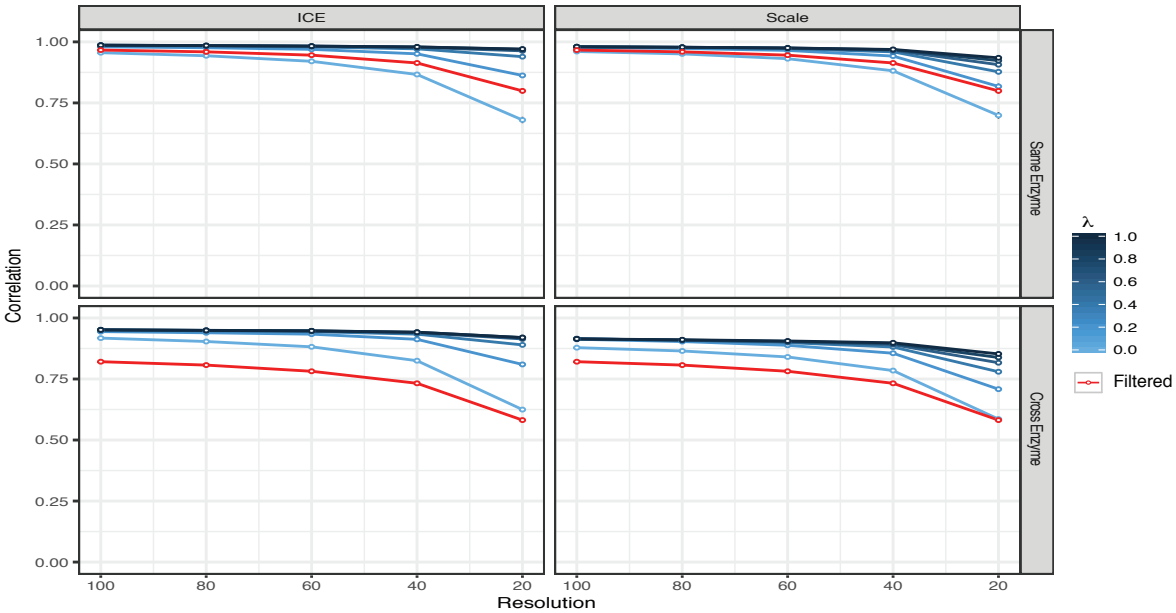
ICE
Scale
Same Enzyme
Cross Enzyme
Correlation
1.00
0.75
0.50
0.25
0.00
100
80
60
40
20
Resolution
λ
1.0
0.8
0.6
0.4
0.2
0.0
Filtered

c

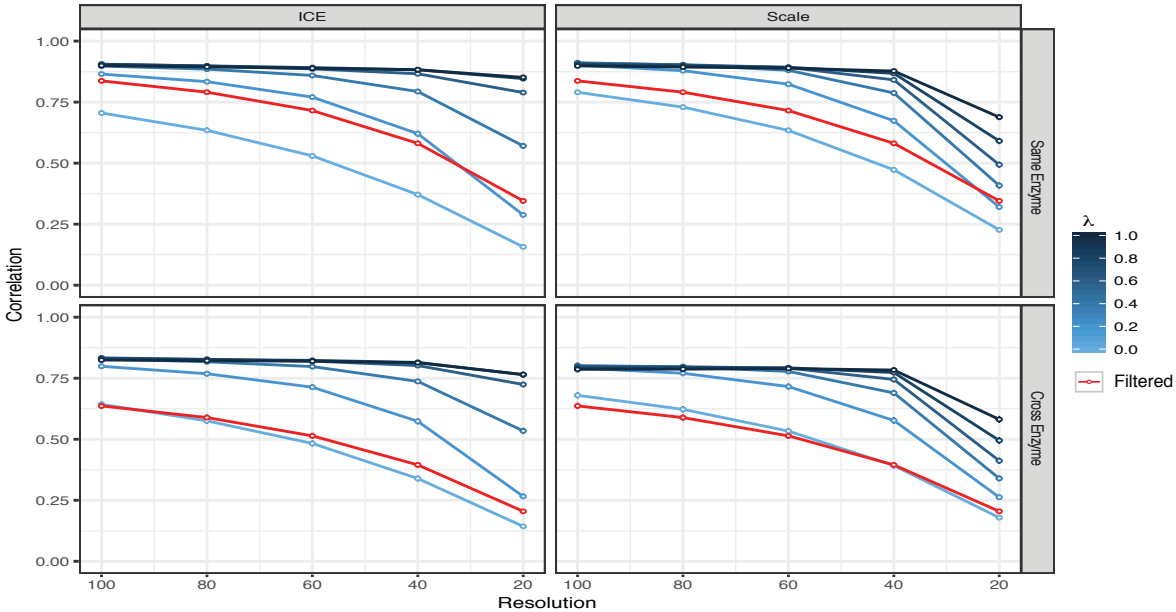
ICE
Scale
Same Enzyme
Cross Enzyme
Correlation
1.00
0.75
0.50
0.25
0.00
100
80
60
40
20
Resolution
λ
1.0
0.8
0.6
0.4
0.2
0.0
Filtered

Figure 3

a

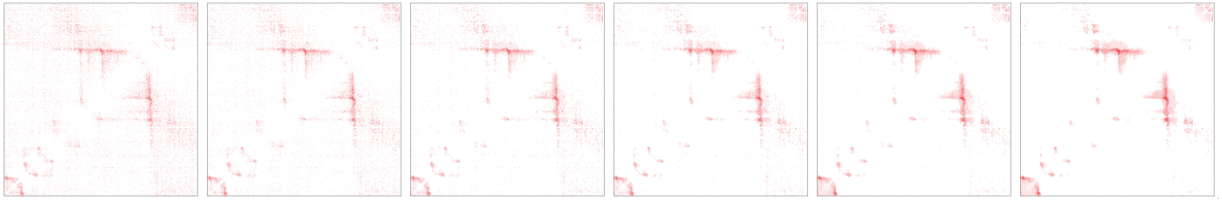

b

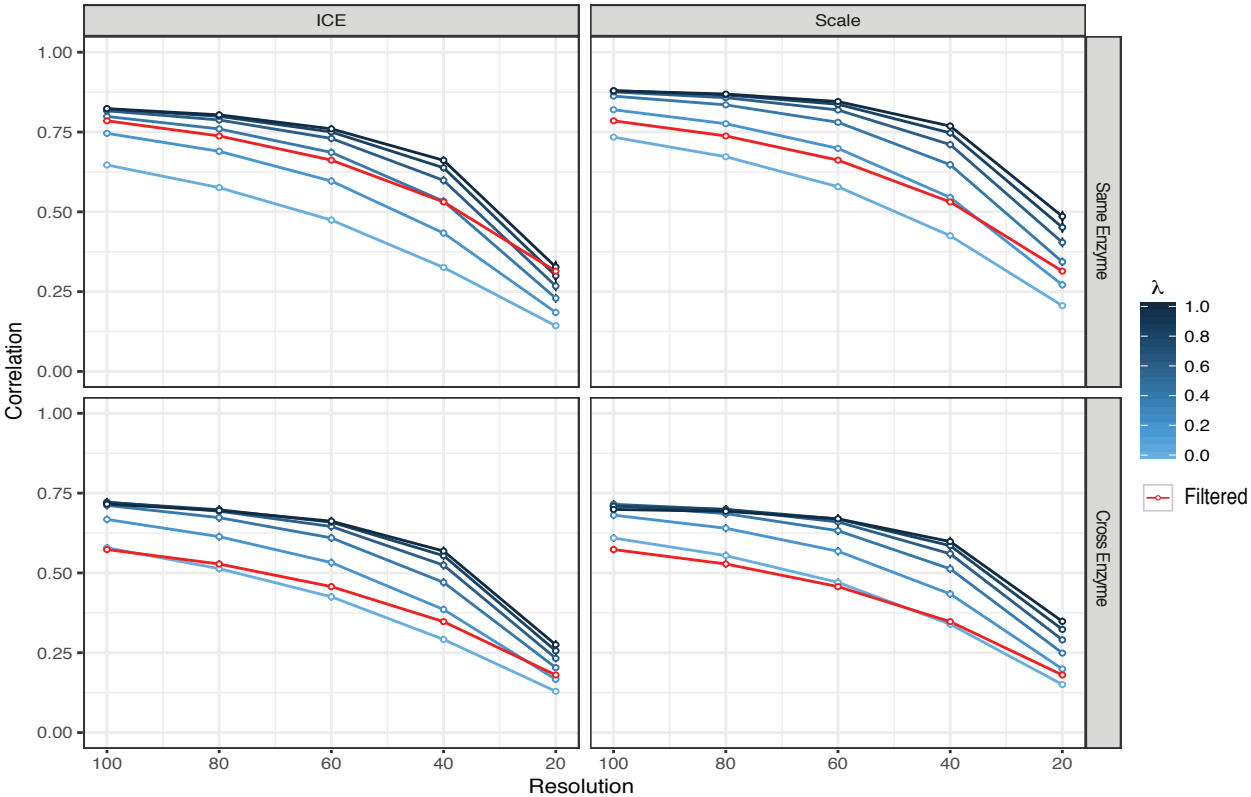
ICE
Scale
Same Enzyme
Cross Enzyme
Correlation
1.00
0.75
0.50
0.25
0.00
100
80
60
40
20
Resolution
λ
1.0
0.8
0.6
0.4
0.2
0.0
Filtered

Figure 4

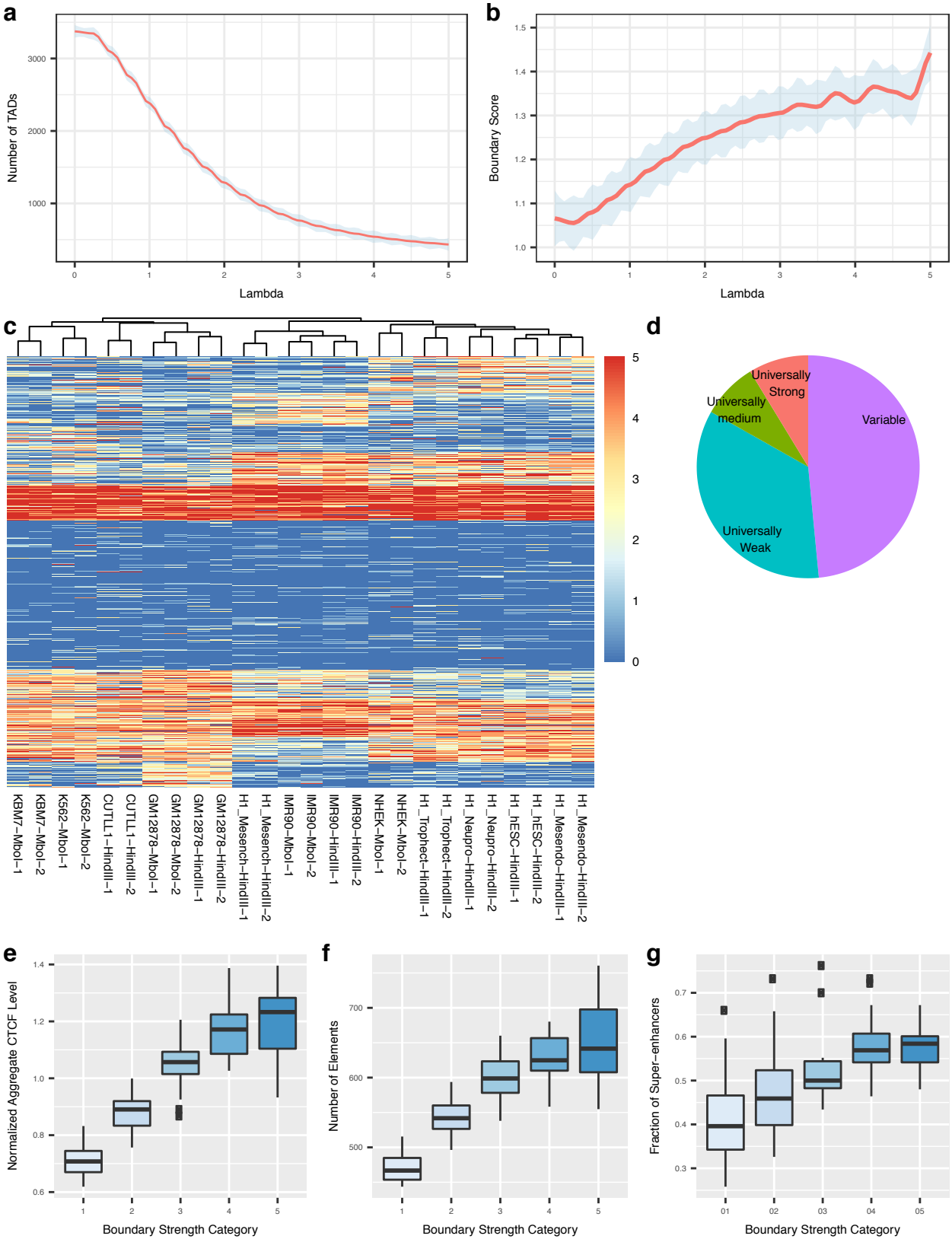
a
Number of TADs
3000
2000
1000
0
1
2
3
4
5
Lambda
b
Boundary Score
1.5
1.4
1.3
1.2
1.1
1.0
0
1
2
3
4
5
Lambda
c
5
4
3
2
1
0
KBM7−MboI−1
KBM7−MboI−2
K562−MboI−1
K562−MboI−2
CUTLL1−HindIII−1
CUTLL1−HindIII−2
GM12878−MboI−1
GM12878−MboI−2
GM12878−HindIII−1
GM12878−HindIII−2
H1_Mesench−HindIII−1
H1_Mesench−HindIII−2
IMR90−MboI−1
IMR90−MboI−2
IMR90−HindIII−1
IMR90−HindIII−2
NHEK−MboI−1
NHEK−MboI−2
H1_Trophect−HindIII−1
H1_Trophect−HindIII−2
H1_Neupro−HindIII−1
H1_Neupro−HindIII−2
H1_hESC−HindIII−1
H1_hESC−HindIII−2
H1_Mesendo−HindIII−1
H1_Mesendo−HindIII−2
d
Universally Strong
Universally medium
Variable
Universally Weak
e
Normalized Aggregate CTCF Level
1.4
1.2
1.0
0.8
0.6
1
2
3
4
5
Boundary Strength Category
f
Number of Elements
700
600
500
1
2
3
4
5
Boundary Strength Category
g
Fraction of Super−enhancers
0.7
0.6
0.5
0.4
0.3
01
02
03
04
05
Boundary Strength Category

Supplementary Figure 1

a

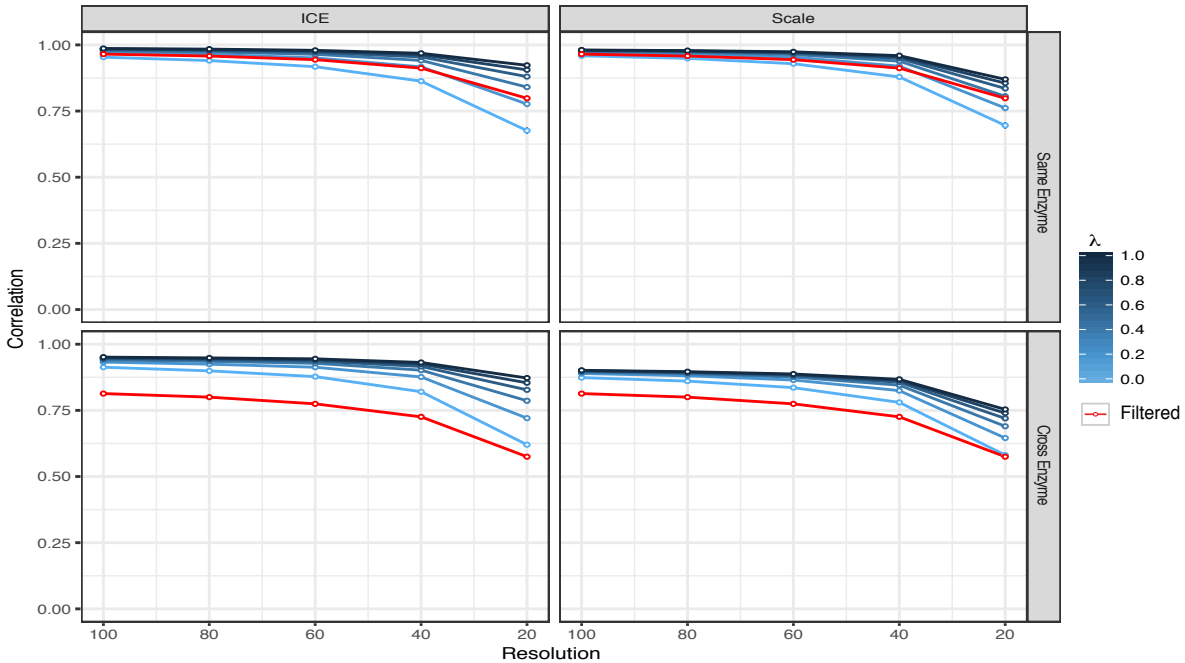

b

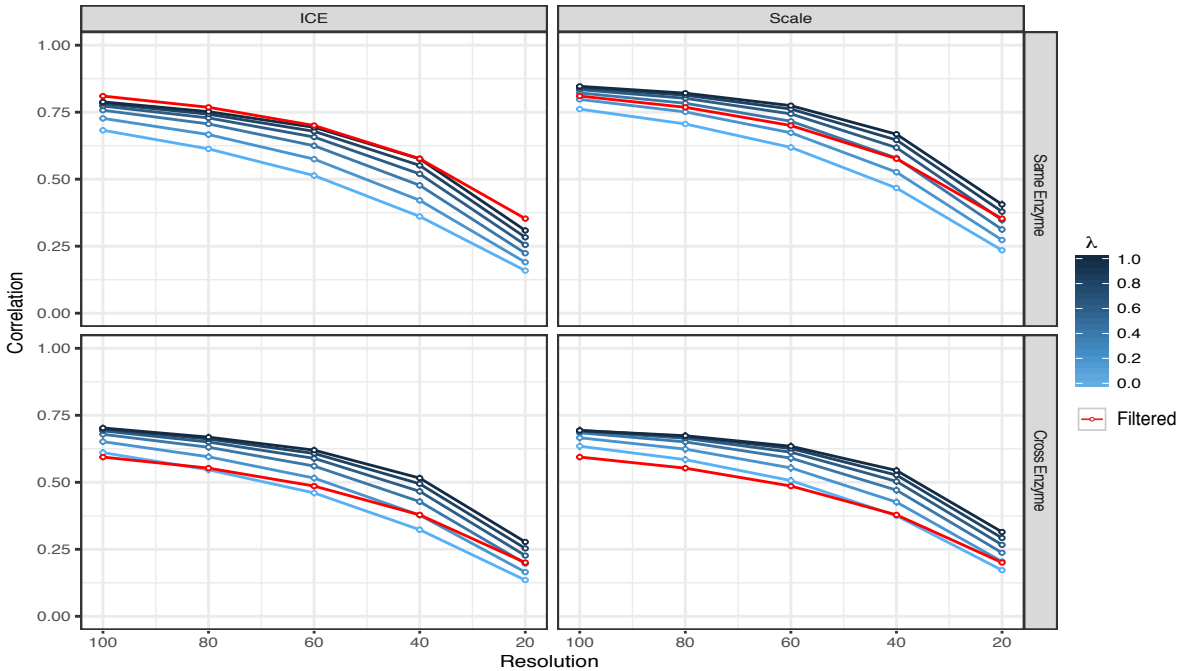

Supplementary Figure 2

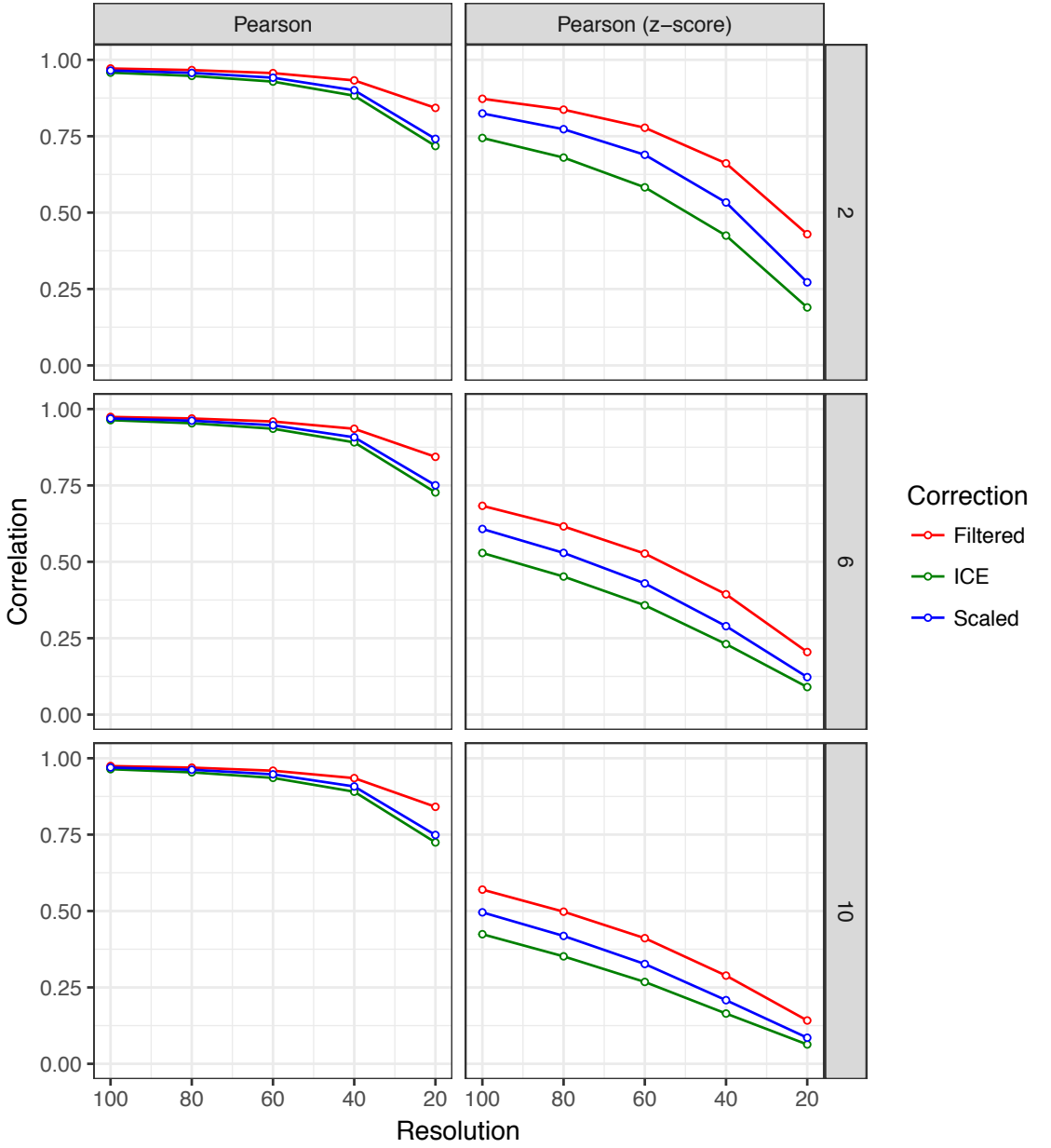

Supplementary Figure 3

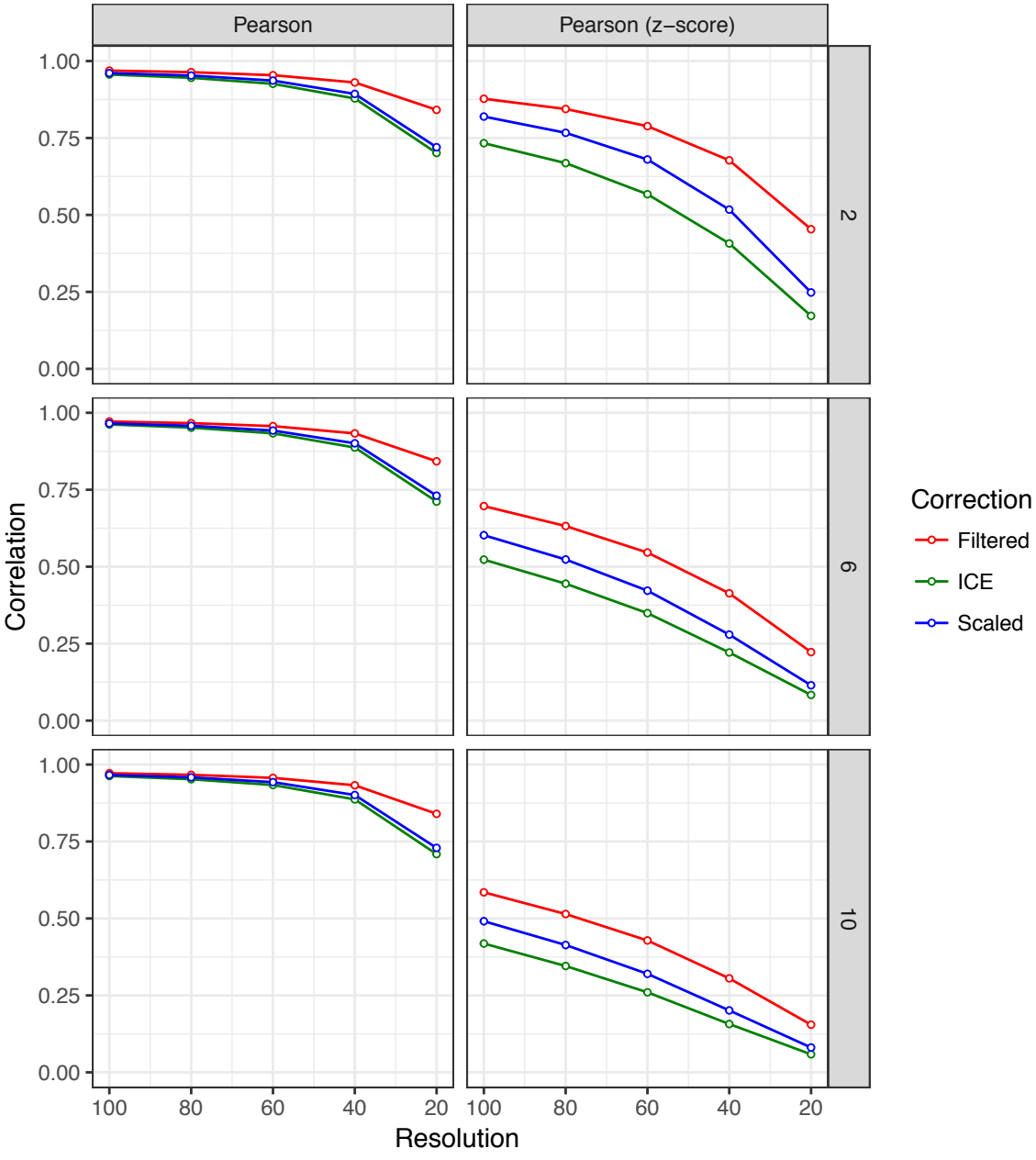
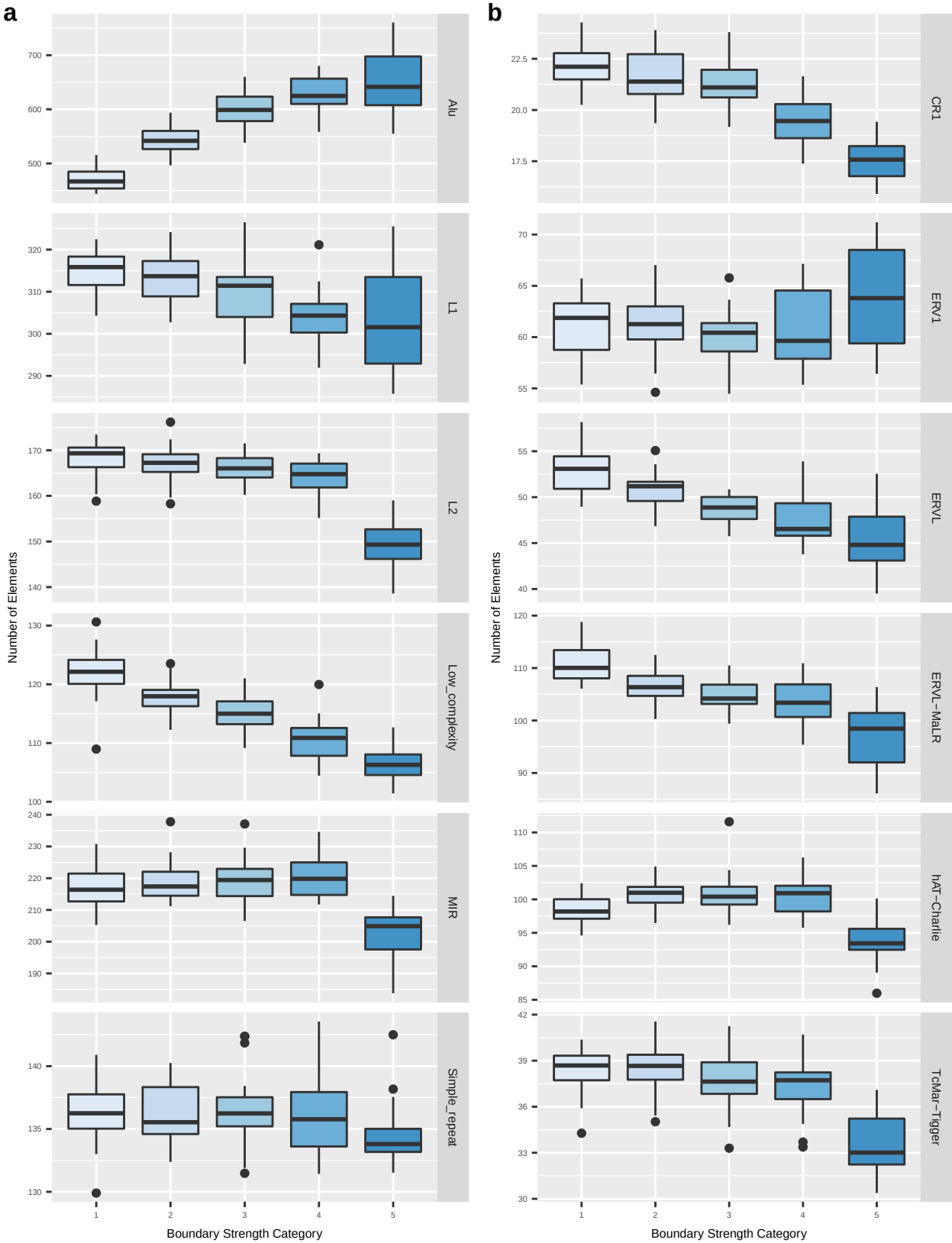
Supplementary Figure 4